Materials Advances

ROYAL SOCIETY OF CHEMISTRY

PAPER

View Article Online
View Journal | View Issue

Cite this: *Mater. Adv.*, 2022, 3, 3316

The fabrication of a highly conductive ceria-embedded gadolinium-stabilized bismuth oxide nanocomposite solid electrolyte for low-temperature solid oxide fuel cells†

Abjana Parbin and Rafiuddin *

Received 29th December 2021,
Accepted 25th February 2022

DOI: 10.1039/d1ma01254a

rsc.li/materials-advances

We report the synthesis of a nanocomposite solid electrolyte, $(1-x)Bi_2O_3$–Gd_2O_3:$xCeO_2$ (GDBC), made up of ceria-embedded gadolinium-stabilized bismuth oxide (Bi_2O_3–Gd_2O_3, GDB) for low-temperature solid oxide fuel cell (LT-SOFC) applications. Different compositions of $(1-x)Bi_2O_3$–Gd_2O_3:$xCeO_2$ (where $0 \leq x \leq 50$ wt%) were fabricated using a solid-state method. Detailed structural analysis of the nanocomposite solid electrolyte samples was done using SEM, TEM, XRD, and FT-IR techniques. The incorporation of CeO_2 nanofiller enhances the ionic conductivity relative to Bi_2O_3–Gd_2O_3 nanocomposite solid electrolyte *via* creating new routes for oxygen-ion conduction within the parent network. Among the different compositions of nanocomposite material, GDBC with 40 wt% CeO_2 nanofiller shows the maximum ionic conductivity, *i.e.*, $\sigma = 7.56 \times 10^{-2}$ S cm^{-1}, and lowest activation energy (0.0954 eV) at low temperature (340 °C). Notably, challenges preventing the commercialization of LT-SOFCs include material conductivity, safety, and production costs. Hence, this superionic nanocomposite solid electrolyte with 40 wt% CeO_2, having high conductivity at low temperature and low cost, could be a promising candidate for the fabrication of electrolytes for fuel-cell applications.

1. Introduction

The widespread use of renewable energy sources is entirely dependent on the development of efficient energy storage technologies. Stable batteries that can be safely operated and have high specific capacities are required to support environmentally friendly electric vehicles and grid storage.[1,2] Liquid electrolytes are currently widely utilized in batteries, although they pose safety concerns, such as liquid spillage or ignition. Solid-state materials are much more suitable from the perspectives of device fabrication, stability, and safety.[3] All solid-state batteries have a cathode, anode, and electrolyte, and the qualities of the batteries are mostly determined based on the properties of the electrolyte.[4] As a result, electrolytes with high ionic conductivity are referred to as superionic conductors,[5] and their strong electrochemical stability is predicted to create favorable electrochemical interfaces when coupled with appropriate electrodes.[6] Solid electrolytes and superionic conductors have been investigated extensively to address the inherent issues mentioned above. Sensors, solid oxide fuel cells, capacitors, and solid-state batteries all make use of them.[7] To date, the exploration and development of electrode materials for use with high-performance superionic conductors have received a lot of interest.

Solid oxide fuel cells (SOFCs) are sophisticated electrochemical energy-conversion devices that convert chemical energy directly into electrical energy.[8] They have excellent prospects for addressing the increasing demands for energy because of their high conversion efficiencies, low emissions, zero noise, and wide application potential.[9] Solid oxide fuel cells (SOFCs) have drawn much interest as they are ecologically benign, highly efficient, and show excellent ionic conductivity. Zirconia doped with 8% yttria (YSZ) has been regarded as the best electrolyte.[10–12] However, the high working temperature poses several issues, including material deterioration and the need for costly noble-metal electrodes.[13] Solid electrolytes exhibiting high ionic conductivity in the low temperature range (below 600 °C) must be developed.

Nanoparticles of bismuth sesquioxide (Bi_2O_3) are frequently utilized as a fundamental precursor of various solid electrolytes.[14] Many researchers have investigated the electrical conduction of pure Bi_2O_3 and found that α-Bi_2O_3 has poor conductivity, whereas δ-Bi_2O_3 exhibits significant oxide-ion conductivity at high temperatures due to the number of oxygen-ion vacancies in its defective fluorite-type structure.[15]

Physical Chemistry Division, Department of Chemistry, Aligarh Muslim University, Aligarh, 202002, India. E-mail: rafiuddin.chem11@gmail.com

† Electronic supplementary information (ESI) available. See DOI: 10.1039/d1ma01254a

At high temperatures, bismuth sesquioxide tends to reduce under low oxygen pressure. However, as mentioned above, high operating temperatures pose challenges, including material deterioration and the need for costly noble-metal electrodes. As a result, reducing the operating temperature below 600 °C is a growing aim.[13] Despite several drawbacks, the rapid ionic conduction of δ-Bi_2O_3 and similar materials means they are regarded as potential electrolytes for use in low-temperature solid oxide fuel cells (LT-SOFCs) and moderate-temperature oxygen sensors. As a result, significant research effort has been directed toward stabilizing δ-Bi_2O_3 and improving the chemical and structural stabilities of bismuth-based electrolytes.[16] Thus, to use Bi_2O_3 as a solid electrolyte in fuel cells, the high-temperature cubic phase must be stabilized. Due to the comparable charges of Bi^{3+} and rare-earth doped metals, the use of their composites has been shown to be an appealing solution for this.[17] It is widely known that the ionic radius and polarizability of dopants impact the conductivity and stability of bismuth-oxide-based electrolytes, and these two characteristics are linearly connected for the lanthanide dopants that have been studied. Dopants with a smaller ionic radius than Bi^{3+} (1.17 Å) are commonly employed to stabilize cubic bismuth oxides at room temperature.[18,19] Rare earth elements have high chemical stabilities and melting points and high adsorption capacities for other elements. Under harsh conditions, Gd_2O_3 exhibits strong oxidation resistance, steady chemical activity, and impact resistance.[20] As a result, adding 40 wt% Gd_2O_3 (the ionic radius of Gd^{3+} is 1.078 Å) to the material can significantly improve its performance.[15] Although this substitution stabilizes the fast ionic conducting phase, the increased reactivity and the structural and chemical stabilities under heat cycling and repeated exposure to decreasing oxygen partial pressure are key concerns relating to practical use in SOFCs.[21] To address the issue of reduction-induced electrolyte deterioration, the addition of nanofillers, such as CeO_2, has been studied.[22,23]

In the present work, gadolinium-stabilized bismuth oxide (GDB) incorporating different amounts of CeO_2 (x), abbreviated as GDBC, is reported. A series of homogeneous samples has been prepared *via* a direct mixing method and the samples were characterized *via* SEM, TEM, XRD, FT-IR, and impedance spectroscopy analysis. Electrochemical studies have been done to explore the use of these materials in LT-SOFCs.

2. Experimental section

2.1. Sample fabrication

Pellets of Bi_2O_3–Gd_2O_3–CeO_2 (GDBC) were fabricated for electrochemical studies *via* a solid-state reaction. A stoichiometric mixture of Bi_2O_3 (Fisher Scientific, 99%) and Gd_2O_3 (SRL, extra pure) with a wt% ratio of 3 : 2 was taken and finely ground in an agate mortar in acetone medium for 2 h to obtain a homogeneous mixture. This mixture was then calcined at 800 °C for 10 h in a muffle furnace and allowed to cool down to room temperature, and the final material was ground into fine powder. A series of $(1 - x)Bi_2O_3$–Gd_2O_3:$xCeO_2$ (where $0 \leq x \leq 50$ wt%) materials was prepared *via* a solid-state reaction. For the composite material, the required amount of CeO_2 (Sigma Aldrich, nanopowder, <25 nm) was added to the parent solid electrolyte and this was then thoroughly ground to a fine powder and kept in a muffle furnace at 800 °C for 8 h; finally, the material was hand-ground and pressed into a cylindrical shape (radius: 0.65 cm, thickness: 0.2 cm) under 5 MPa pressure using a hydraulic press.

2.2. Sample characterization

Microscopic analyses of nanocomposite solid electrolyte pellets were carried out using a JEOL JSM-6510LV scanning electron microscope at an accelerating voltage of 20 kV and using a JEOL JEM-2100 transmission electron microscope. Powder X-ray diffractometry (PXRD) analysis was carried out to analyze the crystal phases of samples using a Shimadzu-6100 powder X-ray diffractometer in a Bragg angle range from 5° to 80° at room temperature using Cu kα radiation (λ = 1.5406 Å). To confirm the formation of composites, Fourier-transform infrared (FT-IR) spectroscopy analysis was carried out using a PerkinElmer spectrometer (version 10.03.09). The thermal stability of the nanocomposites was investigated using TGA/DTA (Shimadzu DTG-60 H) under an inert nitrogen atmosphere from 30 to 800 °C. The density of the solid electrolyte was calculated *via* the Archimedes method in deionized water.

3. Results and discussion

3.1. Characterization of $(1 - x)Bi_2O_3$–Gd_2O_3:$xCeO_2$ nanocomposite solid electrolyte

Fig. 1 depicts typical SEM images of Bi_2O_3, Gd_2O_3, CeO_2, and Bi_2O_3–Gd_2O_3 (GDB), and the Bi_2O_3–Gd_2O_3–CeO_2 (GDBC) nanocomposite solid electrolyte. Fig. 1(a)–(c) depicts SEM images of pristine Bi_2O_3, Gd_2O_3, and CeO_2 before calcination. The pristine Bi_2O_3 sample shows densely packed nanorod bundles (Fig. 1(a)). The particles have sharp edges and angular form, as seen in SEM micrographs. The pristine Gd_2O_3 sample involves spheroid-like agglomerates with clear-edged boundaries and sizes ranging from approximately 0.6 to 0.7 μm (see Fig. 1b). An SEM image of pristine CeO_2 nanoparticles is depicted in Fig. 1(c). Most particles are spherical, but some are elongated in form, and these particles are highly accumulated. However, after calcination, GDB (Fig. 1d) and the final Bi_2O_3–Gd_2O_3–CeO_2 (Fig. 1e) nanocomposite solid electrolyte have different morphologies than the pristine materials. The surface morphology of $60Bi_2O_3$–Gd_2O_3:$40CeO_2$ (Fig. 1e) shows that the doped materials (CeO_2 and Gd_2O_3) are clearly embedded into the Bi_2O_3 matrix, which can also be seen based on the elemental mapping results in Fig. S1 (ESI†). The average grain size of the nanocomposite solid electrolyte was determined using IMAGEJ software. The average grain size of the GDB nanocomposite was found to be 1.61 μm and that of the GDBC nanocomposite solid electrolyte with 40 wt% CeO_2 was found to be around 1.4 μm. The density of the GDB

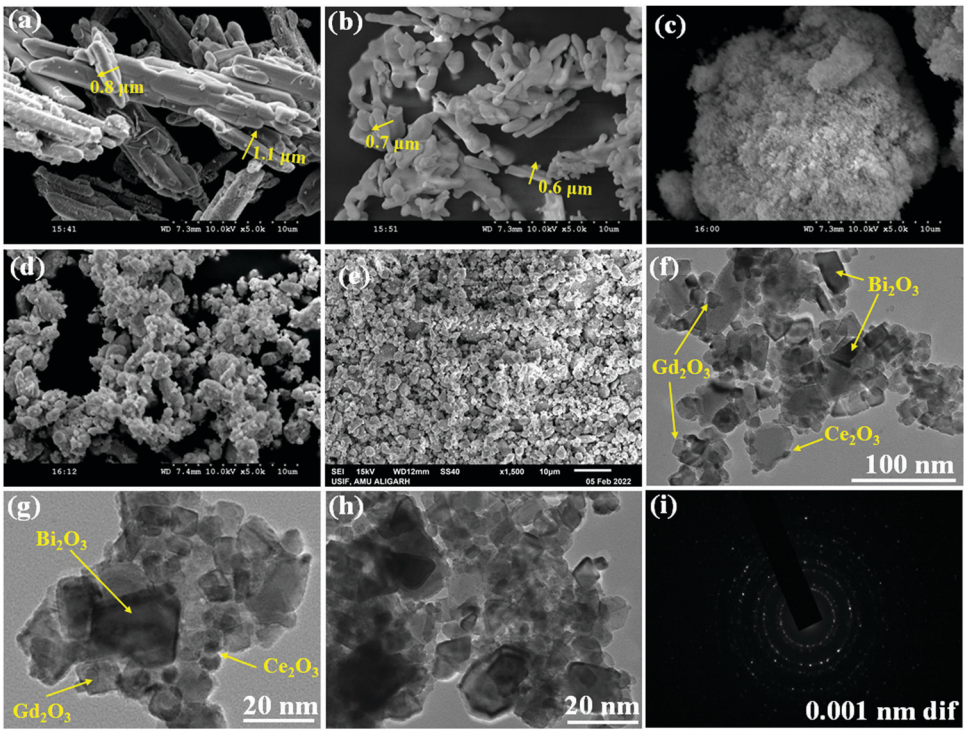

Fig. 1 Structures and morphologies of the as-prepared compounds. SEM images of (a) Bi_2O_3, (b) Gd_2O_3, (c) CeO_2, (d) Bi_2O_3–Gd_2O_3, and (e) $60Bi_2O_3$–Gd_2O_3:$40CeO_2$. (f)–(h) TEM images and (i) the SAED pattern of $60Bi_2O_3$–Gd_2O_3:$40CeO_2$ nanocomposite solid electrolyte.

nanocomposite was 5.044 g cm^{-3}, whereas the density of the GDBC nanocomposite solid electrolyte with 40 wt% CeO_2 was 5.72 g cm^{-3}. TEM observations confirmed the above-mentioned morphological differences. The final Bi_2O_3–Gd_2O_3–CeO_2 nanocomposites have spherical-like structures with unorganized arrangements. Micrographs depict the consistent arrangement and embedding of CeO_2 nanoparticles in the matrix, as shown in Fig. 1(e).

GDBC nanocomposite solid electrolyte with 40 wt% CeO_2 was analyzed *via* TEM to understand the structural characteristics and confirm the generation of a nanocomposite material. It can be seen in Fig. 1(f)–(h) that the nanocomposite material comprised the cubic-like structure of δ-Bi_2O_3 and c-Gd_2O_3, matching well with the XRD results, and this confirms the formation of the material. The TEM images of 40 wt% CeO_2 nanocomposite solid electrolyte illustrated in Fig. 1(f)–(h) reveal the embedded CeO_2 nanoparticles on the surface of Bi_2O_3–Gd_2O_3, which are in touch with one another. Furthermore, the selected area electron diffraction (SAED) pattern displayed in Fig. 1(i) exhibits concentric rings, indicating the polycrystalline structure of the nanocomposite solid electrolyte.

The spatial distributions of different elements in the GDBC nanocomposite solid electrolyte with 40 wt% CeO_2 were investigated *via* elemental mapping analysis (Fig. S1, ESI†). These images indicate that the Ce, Gd, Bi, and O elements are distributed throughout the entire nanocomposite.

The structural phases and crystallinity of Bi_2O_3, Gd_2O_3, CeO_2, GDB, and the GDBC nanocomposite solid electrolyte calcined at 800 °C were studied *via* XRD, and the patterns are depicted in Fig. 2. The diffraction peaks obtained at 2θ values of 27.96° (111), 32.96° (200), 46.36° (220), and 55.15° (311) can be attributed to the planes of cubic δ-Bi_2O_3 (JCPDS card number: 27-0052).[24] The diffraction peaks of Gd_2O_3 obtained at 2θ values of 20.16° (211), 28.62° (222), 33.26° (400), 47.48° (440), and 56.52° (622) can be attributed to the cubic phase of Gd_2O_3 (JCPDS card no: 12-0797).[25] Furthermore, the CeO_2 sample reveals diffraction peaks at 28.56°, 33.44°, 47.87°, 56.50°, and

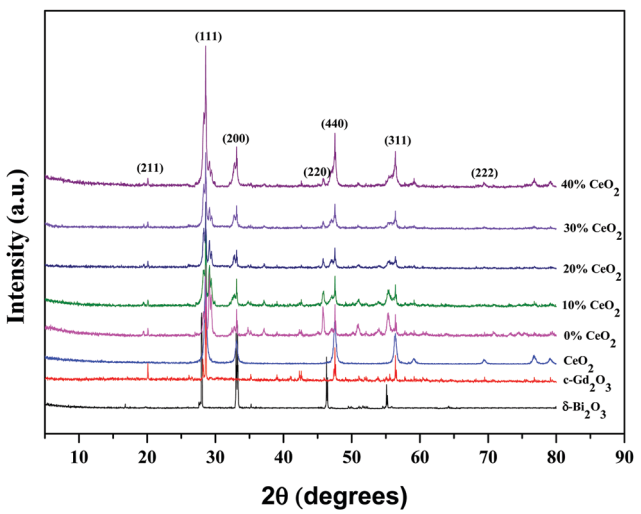

Fig. 2 X-ray diffraction patterns of δ-Bi_2O_3, c-Gd_2O_3, CeO_2, and (1 − *x*)Bi_2O_3–Gd_2O_3:*x*CeO_2 nanocomposite solid electrolyte samples with different wt% levels of CeO_2 nanofiller.

69.80° which correspond to the (111), (200), (220), (311), and (222) planes, respectively (JCPDS card no: 34-0394).[26]

Peaks from both δ-Bi_2O_3 and c-Gd_2O_3 particles coexist in the GDB material and match well with the JCPDS numbers of the individual components. Diffraction peaks from Bi_2O_3, Gd_2O_3, and CeO_2 can be clearly seen in the GDBC nanocomposite solid electrolyte patterns, indicating the successful formation of GDBC nanocomposite solid electrolytes. The diffraction peaks of the as-synthesized Bi_2O_3–Gd_2O_3–CeO_2 nanocomposite solid electrolytes are quite comparable to those of the pure pristine materials, although they are much wider than those of the pristine materials. This suggests that the final products may have a smaller particle size and that their diffraction peaks might overlap.[27] Moreover, the main diffraction peak positions of Bi_2O_3–Gd_2O_3 and CeO_2 are quite similar. It was observed that with an increase in the concentration of CeO_2, the intensity of the CeO_2(311) diffraction peak also increased simultaneously, while the Bi_2O_3(220) and (311) peak intensities decreased, indicating that CeO_2 has been successfully incorporated into the nanocomposite solid electrolyte.[28]

FT-IR spectroscopy was used to distinguish the different functional groups of as-synthesized samples. Fig. 3 depicts the FTIR spectra of pure GDB and GDBC nanocomposite solid electrolyte. The absorption peak at 847.13 cm^{-1} is attributed to Bi–O stretching vibrations.[29] The absorption peak at 1040.77 cm^{-1} is attributed to the bending vibrations of Bi–O bonds.[30] The absorption peaks at 1382 cm^{-1} and 1634.25 cm^{-1} indicate the existence of carbon–oxygen double-bond stretching vibrations of absorbed CO_2.[31] The absorption peak at 541.31 cm^{-1} corresponds to Gd–O vibrations.[32] The strong absorption peak at around 476.43 cm^{-1} is due to O–Ce–O vibrations.[33] The broad absorption peak at 3426.31 cm^{-1} is attributed to the O–H stretching vibrations of water molecules that the nanocomposite solid electrolyte absorbed from surrounding moisture,[34] and the peak at 2921.9 cm^{-1} is attributed to the presence of atmospheric CO_2 in the sample.[35] All the mentioned peaks confirm the formation of CeO_2-embedded Bi_2O_3–Gd_2O_3 nanocomposite solid electrolyte.

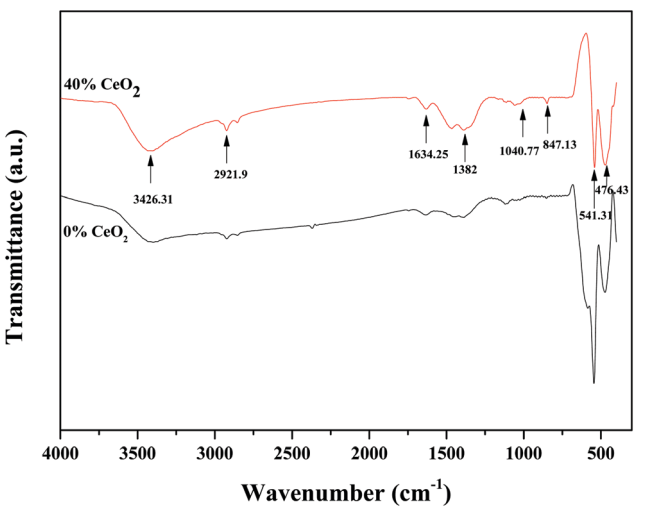

Fig. 3 FT-IR spectra of GDB and GDBC nanocomposite solid electrolyte with 40 wt% CeO_2.

The thermal stability of the synthesized GDBC nanocomposite solid electrolyte with 40 wt% CeO_2 was studied *via* TGA/DTA under an inert nitrogen atmosphere, which is shown in Fig. S2 (ESI†). Approximately 0.8% weight loss from the nanocomposite is detected before 200 °C, and this is mostly due to the removal of moisture. A further decrease in the TGA curve indicates weight loss of 2% from the nanocomposite material, which is attributed to the removal of lattice water in the temperature range of 300–480 °C.[36] As shown in the plot, the sample is stable from 500 °C to 800 °C, as revealed by the small weight loss from the nanocomposite. A strong endothermic peak is observed at 700–750 °C in the DTA curve, which shows a Bi_2O_3 phase transformation from the α phase to the δ phase.

3.2. Electrochemical characterization of $(1-x)Bi_2O_3$–Gd_2O_3:$xCeO_2$ nanocomposite solid electrolyte: analysis of impedance spectra and an evaluation of conductivity

Nanocomposite pellets with a thickness of 0.2 cm were used for electrochemical tests. For better electrical connectivity between the sample and electrodes, the pellets were coated with silver paste. AC impedance measurements were carried out using the pellets over a frequency range of 20 Hz–1 MHz at various temperatures under an air atmosphere. The electric and dielectric properties of the samples were also studied using the same instrument.

AC complex impedance spectroscopy is a popular non-destructive method for the analysis of the electrical processes and conductive mechanisms related to crystalline materials.[37] Cole–Cole plots of $(1-x)Bi_2O_3$–Gd_2O_3:$xCeO_2$ solid electrolyte samples at 613 K are depicted in Fig. 4. AC complex impedance spectroscopy is a diagnostic tool for separating the contributions of grains, grain boundaries, and the electrode–electrolyte interface.[38]

Impedance data are illustrated in the form of imaginary z'' (capacitive) impedance against real z' (resistive) impedance. The Cole–Cole plots show typical impedance spectra shapes that consist of a semicircular arc in the higher frequency range, which is attributed to resistive (R) and capacitive (C) components,[39] and an inclined spike in the lower frequency range, which is attributed to electrode processes.[8,40] The low frequency spike is ascribed to ionic conductivity while the high frequency semicircle is ascribed to the effects of grain boundaries.[41]

From Fig. 4, it is noted that the radius of the grain boundary arc of the nanocomposite solid electrolyte decreases as the concentration of CeO_2 nanofiller is increased. It is found that the radius of the semicircle is minimum for $(1-x)Bi_2O_3$–Gd_2O_3:$xCeO_2$ when x = 40 wt%, and the radius increases with further increases in the CeO_2 content. The reason for this behavior may be an increase in the number of carrier ions and ionic mobility for 40 wt% CeO_2, thus leading to a decline in the bulk resistance.[42]

The ionic conductivities of the nanocomposite materials with various concentrations of CeO_2 can be evaluated using the following formula:

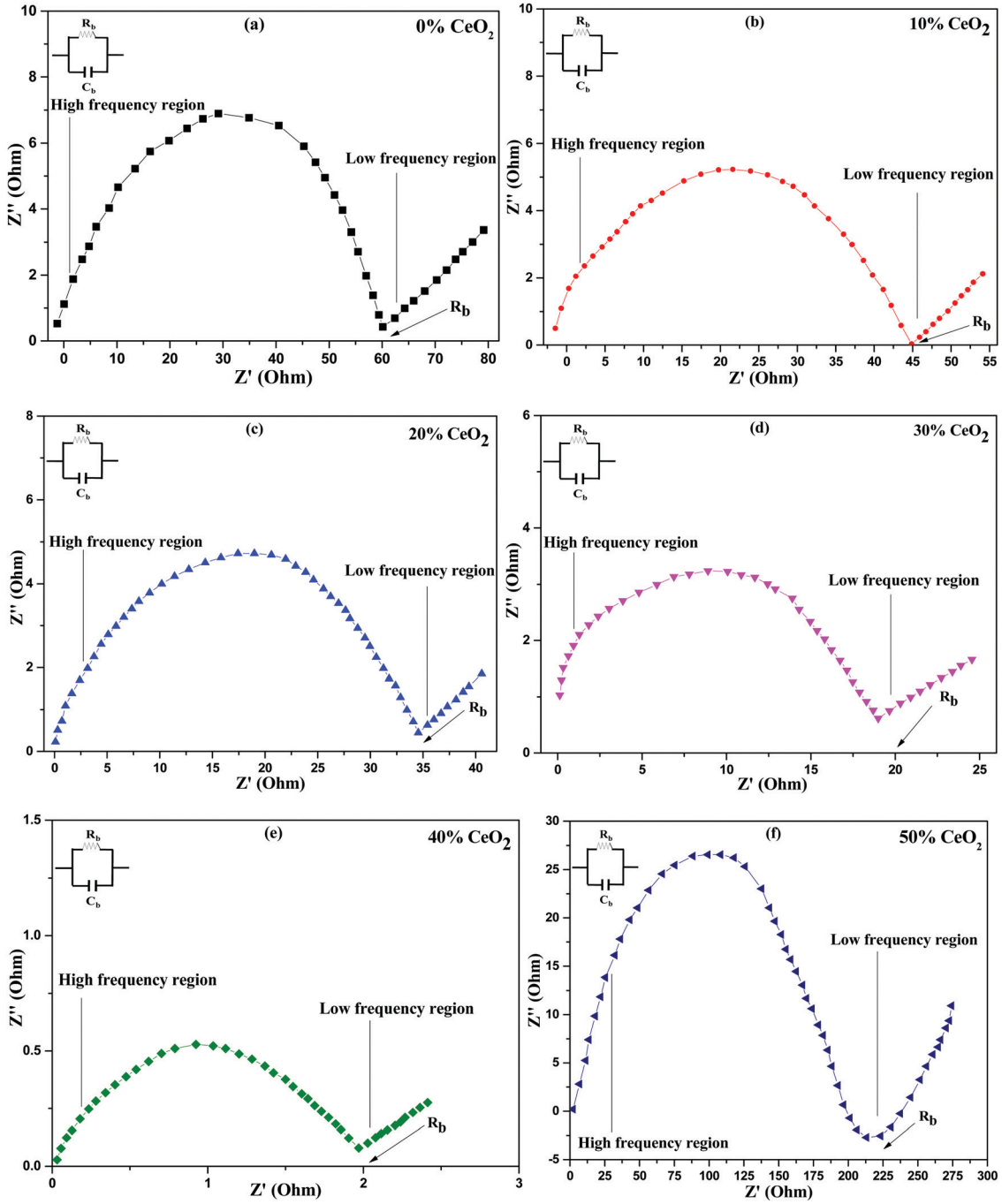

Fig. 4 Cole–Cole (complex impedance) spectra of $(1 - x)Bi_2O_3–Gd_2O_3:xCeO_2$ nanocomposite solid electrolyte samples with different wt% levels of CeO_2 at a temperature of 613 K.

$$\sigma = L/(R \times S) \quad (1)$$

where L is the thickness of the pellet in cm, R is the bulk resistance in Ω, and S is the area of the pellet in cm^2.[2]

Conductivity measurements were carried out on all synthesized nanocomposite materials to analyze the nature of conduction in the presence of CeO_2 nanofiller. Impedance spectroscopy data is commonly used to calculate conductivity. This approach is preferred because it prevents electrode polarization and allows for the differentiation of grain and grain-boundary contributions to the total resistance, among other benefits.[43] The intercept of the semicircle with the real axis in the low frequency domain was used to determine the bulk resistance at all concentrations, as shown in Fig. 4.[44] The ionic conductivities of the nanocomposite materials at 613 K are shown in Table 1, where solid electrolyte containing 0 wt% CeO_2 has ionic conductivity ($\sigma = 2.52 \times 10^{-3}$ S cm^{-1}) that is comparable to the value for $Bi_2O_3–Gd_2O_3$ reported by

Table 1 The ionic conductivity values of $(1-x)Bi_2O_3$–Gd_2O_3:$xCeO_2$ nanocomposite solid electrolyte with different wt% levels of CeO_2 at 613 K

Sample	σ (S cm^{-1})
0% CeO_2	2.52×10^{-3}
10% CeO_2	3.3×10^{-3}
20% CeO_2	4.58×10^{-3}
30% CeO_2	8.4×10^{-3}
40% CeO_2	7.56×10^{-2}
50% CeO_2	7.03×10^{-4}

T. Takahashi *et al.*[15] However, the conductivity improves upon increasing the CeO_2 concentration and reaches a maximum for 40 wt% CeO_2 at 613 K (σ = 7.56 × 10^{-2} S cm^{-1}). When we compare the aforementioned conductivity values to the nanocomposite solid electrolytes that we have synthesized, *i.e.*, $(1-x)Bi_2O_3$–Gd_2O_3:$xCeO_2$ with various weight percentages of CeO_2, the difference is enormous. This might be owing to the presence of the nanofiller, which can enhance the ionic transport and the motion of constituent components.[45] This activity is inhibited at a lower temperature but at a higher temperature the host matrix can expand, increasing the overall mobility of the ions and resulting in higher ionic conductivity.[46] The main reasons for using nanofillers are two-fold: (i) to improve the ionic conductivity at low temperatures and (ii) to improve the stability at the electrode–electrolyte interface.[47] Because of heterogeneous doping, ions are drawn to the surface of the dispersoid, resulting in a depletion zone with a higher concentration of ion vacancies. This depletion zone is characterized by a highly conducting space-charge layer that runs along the matrix–particle interface.[40] This study found that conductivity is directly connected to the concentration of nanofiller, *i.e.*, when the CeO_2 wt% increases, the conductivity increases, before passing a threshold value and then decreasing. Defect generation in the interface zone, which is itself a disordered zone, contributes significantly to the high conductivity. The primary role of the nanofiller is to modify ion-ion mobility, which may result in improved ionic transport. This is due to the thermally stimulated process of CeO_2 grains creating new empty sites within the parent network.[42] However, a decrease in ionic conductivity is observed at CeO_2 concentrations greater than 40 wt%. This is because the presence of excess nanofiller in the nanocomposite system can cause ion pairing and aggregation, impeding ionic transport and thus preventing conduction.[48] The obtained conductivity value for 40 wt% CeO_2 appears to be a maximum of 7.56 × 10^{-2} S cm^{-1} at a more useful temperature of 613 K.

Conductivity and activation energy are two major characteristics used to evaluate electrolyte performance. Conductivity measurements were carried out on all the synthesized nanocomposite materials to analyze the nature of conduction in the presence of CeO_2 nanofiller. The conductivities of the nanocomposite solid electrolytes are plotted against the inverse of absolute temperature (T) in Fig. 5. Activation energy is calculated on the assumption that ionic conduction in a solid electrolyte is a thermally stimulated process. In other words, according to an Arrhenius-type equation, the conductivity of an

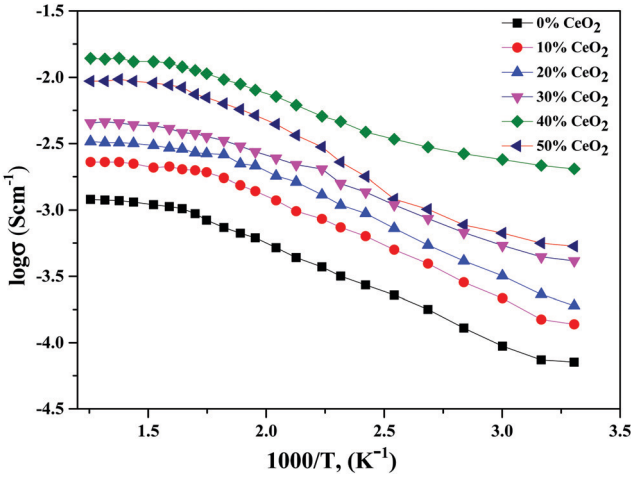

Fig. 5 Variation of ionic conductivity as a function of the inverse of temperature for $(1-x)Bi_2O_3$–Gd_2O_3:$xCeO_2$ nanocomposite solid electrolyte samples with different CeO_2 concentrations.

electrolyte tends to increase with an increase in temperature, as follows:[43]

$$\sigma = \sigma_o \exp\left(\frac{-E_a}{kT}\right) \quad (2)$$

where σ_o is a pre-exponential factor, E_a is the activation energy, T is the absolute temperature, and k is the Boltzmann constant.

Using eqn (2), we can determine E_a based on the regression method across the entire temperature range, and the values of E_a for different wt% levels of CeO_2 nanofiller are shown in Fig. 6. The activation energy decreases from 0.1334 to 0.0954 eV as the CeO_2 nanofiller content increases from 10 to 40 wt%. Then the activation energy increases with increasing CeO_2 content, attaining a value of 0.1444 eV for 50 wt% CeO_2. The lowest activation energy is exhibited by the 40 wt% CeO_2 nanocomposite solid electrolyte: 0.0954 eV. Thus, it can be inferred that ions require only 0.0954 eV of energy to migrate

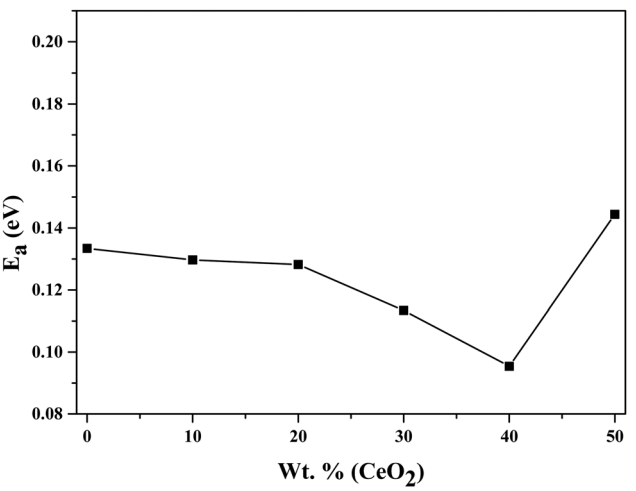

Fig. 6 Variation of the activation energy of $(1-x)Bi_2O_3$–Gd_2O_3:$xCeO_2$ nanocomposite solid electrolyte as a function of CeO_2 wt%.

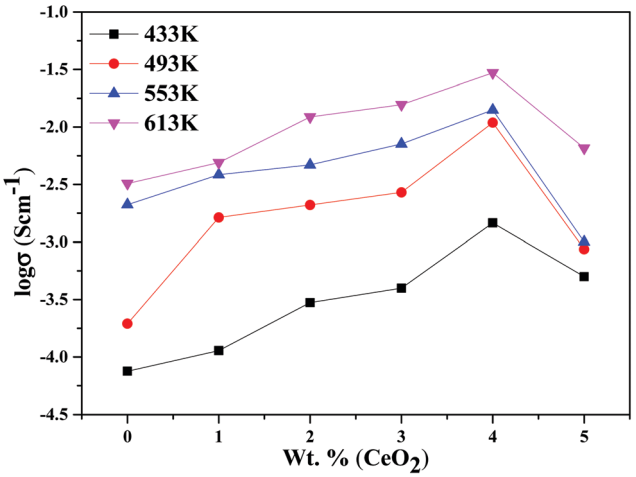

Fig. 7 Ionic conductivities for $(1-x)Bi_2O_3$–Gd_2O_3:$xCeO_2$ nanocomposite solid electrolyte samples as a function of CeO_2 wt% at different temperatures.

from one site to another, indicating that the ions in the nanocomposite solid electrolyte sample are highly mobile.

The decline in ionic conductivity above 40 wt% can also be seen in Fig. 7, which depicts the nanocomposite solid electrolyte ionic conductivity at various temperatures as a function of CeO_2 wt%. Fig. 8 displays the frequency dependence of conductivity (σ) for 40 wt% CeO_2 doped Bi_2O_3–Gd_2O_3 nanocomposite solid electrolyte at various temperatures. Each curve has a low frequency plateau corresponding to the bulk material DC conductivity and a high frequency dispersive portion corresponding to its AC conductivity. The conductivity plots exhibit dispersion, which shifts to a higher frequency as the temperature rises. This behavior implies that ionic conduction in the nanocomposite material proceeds *via* a hopping process, as described by the Jonscher universal power law.[49,50] Fig. 8 shows that σ_{dc} drops with a decrease in frequency and tends to become frequency independent below a specific value.

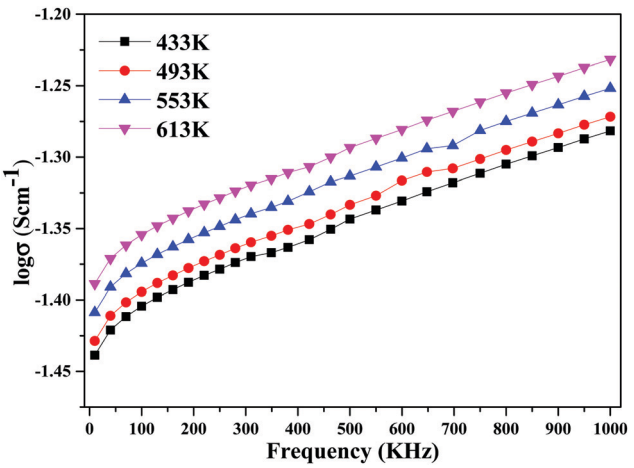

Fig. 8 Variation of ionic conductivity as a function of frequency for $(1-x)Bi_2O_3$–Gd_2O_3:$xCeO_2$ nanocomposite solid electrolyte with 40 wt% CeO_2.

3.3. Dielectric properties of $(1-x)Bi_2O_3$–Gd_2O_3:$xCeO_2$ nanocomposite solid electrolyte

For integrated circuits and sophisticated packaging technologies, the dielectric constant is an essential observable component affecting the design of capacitors, resistors, transformers, and inductors.[51]

The frequency-dependent real part of the dielectric constant (ε') can be calculated using the following equation:

$$\varepsilon' = \frac{C_p t}{\varepsilon_o A} \quad (3)$$

where C_p represents the capacitance of a specimen in Farads (F), t is the thickness, ε_o is the free space permittivity (8.854×10^{-12} F m^{-1}), and A is the area of the pellet.[52]

The imaginary part of the dielectric constant (ε'') can be calculated *via* the following equation:

$$\varepsilon'' = \varepsilon' \tan\delta \quad (4)$$

where $\tan\delta$ is the dielectric loss tangent.[53]

Real and imaginary dielectric constant and dielectric loss values for the selected compositions at various frequencies at a temperature of 613 K are shown in Fig. 9. It is shown that all samples had a high dielectric constant at low frequencies; this dropped as the frequency increased, eventually reaching saturation at higher frequencies. The values of the dielectric constant (real and imaginary parts) improved upon increasing the CeO_2 nanofiller content, reaching a maximum at 40 wt% CeO_2. Following that, when the concentration of CeO_2 was increased further (50 wt% CeO_2), the dielectric constant value fell because mobile oxide ions are unable to travel quickly due to obstruction from conduction channels. The slow movement of ions at a CeO_2 concentration of 50 wt% results in a low dielectric constant value due to reduced conduction-related polarization.[52]

At lower frequencies, the high dielectric constants for all wt% ratios of CeO_2 nanofiller could be linked to a buildup of charge at the sample-electrode interface, which is known as space charge polarization, or it might be due to interfacial polarization, as predicted by Maxwell–Wagner theory. This is characteristic of ion-conducting materials.[53]

Fig. 10 depicts the frequency-dependent tangent loss ($\tan\delta$) of nanocomposite materials with different amounts of CeO_2 at 613 K. The dielectric loss is the amount of energy lost in a dielectric material. It is shown that the value of $\tan\delta$ progressively decreases as the frequency increases. The high value of $\tan\delta$ at low frequency can be related to conductivity relaxation or it may be ascribed to free charge mobility in the material.[54]

The temperature dependence of the dielectric constant at 1 MHz for $(1-x)Bi_2O_3$–Gd_2O_3:$xCeO_2$ nanocomposite solid electrolyte samples is shown in Fig. 11. It is observed that the dielectric constant increases with an increase in temperature for all compositions. This could be due to an increase in oxide-ion mobility through the solid electrolyte, which is thermally activated.[55]

The highest dielectric constant values are observed for the 40 wt% CeO_2 composition over the entire temperature range

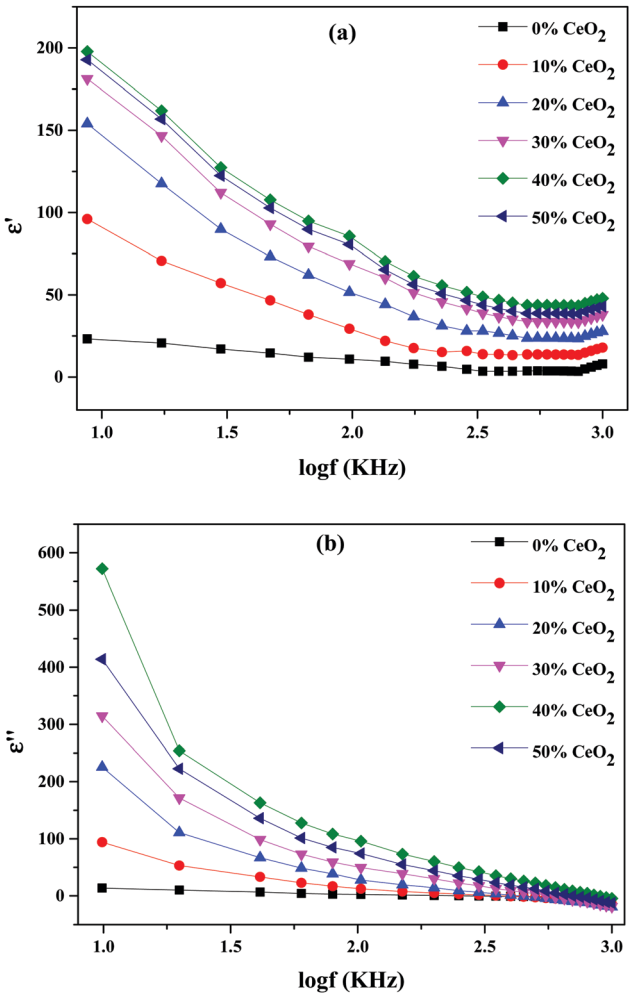

Fig. 9 Variations of (a) the real part of the dielectric constant and (b) the imaginary part of the dielectric constant for $(1-x)Bi_2O_3$–Gd_2O_3:$xCeO_2$ nanocomposite solid electrolyte samples with different CeO_2 concentration levels.

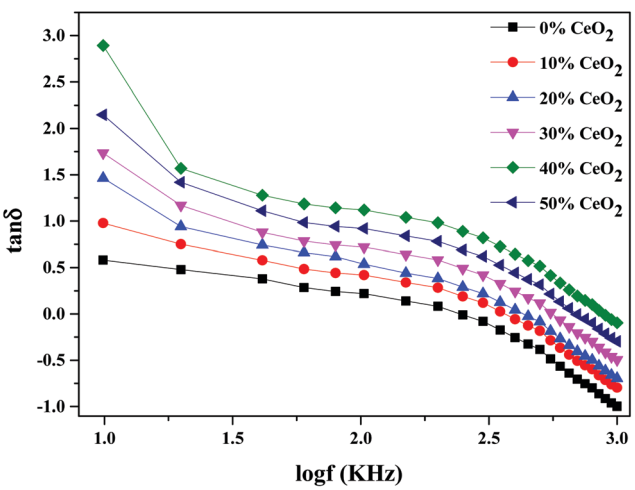

Fig. 10 The variation of dielectric loss as a function of frequency for $(1-x)Bi_2O_3$–Gd_2O_3:$xCeO_2$ nanocomposite solid electrolyte with different amounts of CeO_2 nanofiller.

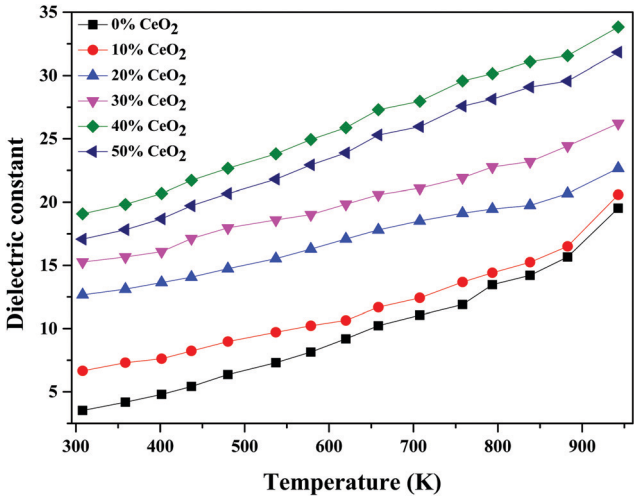

Fig. 11 Temperature-dependent dielectric constant values of $(1-x)Bi_2O_3$–Gd_2O_3:$xCeO_2$ nanocomposite solid electrolyte samples with different CeO_2 concentrations at 1 MHz.

studied. This increase in dielectric constant value can be attributed to the concept of dielectric polarization. At lower temperature, charge carriers cannot always follow the applied field direction, resulting in a weak contribution to polarization and dielectric behavior. As the temperature increases, the charge carriers become excited and have adequate energy to raise the dielectric constant.[56]

As seen in Fig. 12, the dielectric constant decreases with an increase in frequency due to the low polarization. The high dielectric constant values might be due to space-charge polarization caused by ionic transport and structural distortion in the material.[57]

The material dielectric properties have a direct relationship with the AC conductivity, as follows:

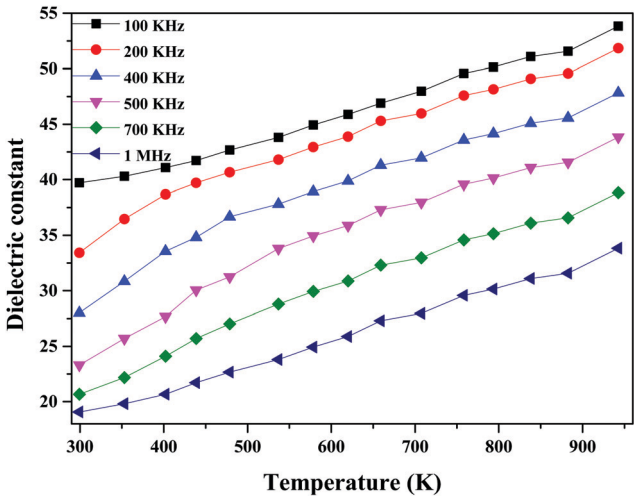

Fig. 12 Dielectric constant values at different frequencies as a function of temperature for $60Bi_2O_3$–Gd_2O_3:$40CeO_2$ nanocomposite solid electrolyte.

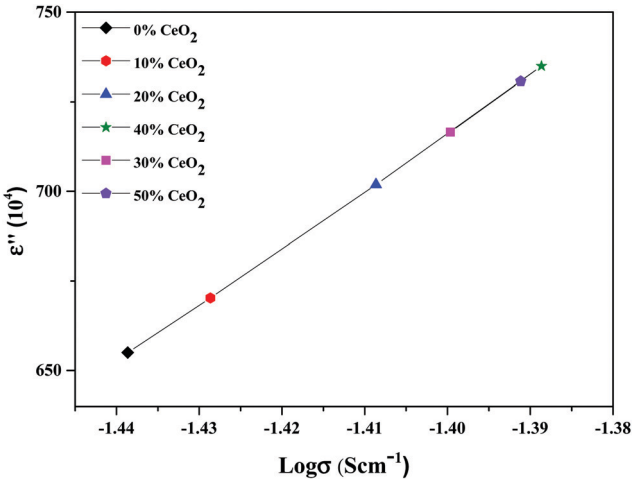

Fig. 13 Variation of the dielectric constant as a function of conductivity for $(1-x)Bi_2O_3$–Gd_2O_3:$xCeO_2$ nanocomposite solid electrolyte samples with different amounts of CeO_2 nanofiller at 10 kHz.

$$\sigma_{AC} = 2\pi f \varepsilon_o \varepsilon'' \quad (5)$$

From the above relationship, it can be inferred that the higher the conductivity, the higher the dielectric constant of the nanocomposite. A higher dielectric constant suggests that a nanocomposite can store more electric potential energy when subjected to an alternating electric field.[58] The conductivities of nanocomposite solid electrolytes with different CeO_2 concentrations against ε'' at a constant frequency of 10 kHz are depicted in Fig. 13. It is shown that the value of conductivity increases with the dielectric constant, and the value was found to be maximum for 40 wt% CeO_2. The concept of dielectric polarization can explain the increase in the dielectric constant value.

The long-term stability of the ionic conductivity of GDBC nanocomposite solid electrolyte with 40 wt% CeO_2 was tested at 613 K using EIS in an open circuit under an air atmosphere, and the results are shown in Fig. 14 as a function of time. While the initial conductivity was marginally reduced during the first 23 h, high ionic conductivity was maintained for more than 100 h without any detectable deterioration, confirming the great stability.

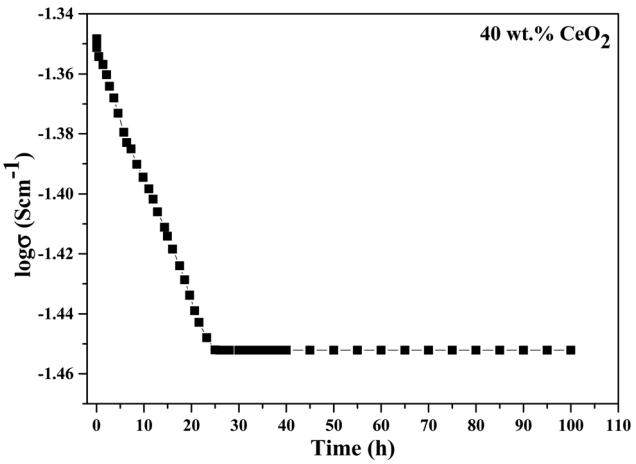

Fig. 14 Long-term stability testing of the conductivity of GDBC nanocomposite solid electrolyte with 40 wt% CeO_2.

4. Conclusions

A simple and low-cost approach for fabricating $(1-x)Bi_2O_3$–Gd_2O_3:$xCeO_2$ nanocomposite solid electrolyte samples using a solid-state method followed by optimum thermal treatment at 800 °C was developed, and the resulting nanocomposite samples were characterized *via* SEM, TEM, XRD, and FT-IR analysis. The ionic conductivity increases significantly upon CeO_2 addition and reaches a maximum value of $\sigma = 7.56 \times 10^{-2}$ S cm^{-1} for $60(Bi_2O_3$–$Gd_2O_3)$:$40CeO_2$ nanocomposite solid electrolyte with 40 wt% CeO_2 nanofiller at 613 K. The enhancement in conductivity is mostly ascribed to increased mobility as a result of structural modifications caused by compositional changes. The activation energy of the most highly conducting sample (40 wt% CeO_2 nanofiller) was found to be 0.0954 eV. Impedance studies reveal the significant role of grain effects on the conduction process. The dielectric constant and dielectric loss values are found to increase with a decrease in the applied frequency and they increase with increasing temperature. The improved electrical and dielectric properties of the synthesized nanocomposite solid electrolyte could further strengthen the practical use of bismuth-based materials in high-performance low-temperature SOFCs.

Author contributions

Abjana Parbin designed the study, conceptualized the ideas, and carried out experimental analysis and the write-up of the scientific findings. Prof. Rafiuddin supervised the writing (review and editing) of this work. Both authors discussed the results and contributed to the final manuscript.

Conflicts of interest

There are no conflicts to declare.

Acknowledgements

The authors are highly obliged to the Chairman, Department of Chemistry, AMU Aligarh for providing research facilities. We express our gratitude to the Departmental Instrumentation facility for XRD and FT-IR assistance. We are also thankful to the USIF, AMU for SEM and TEM facilities. The authors also acknowledge UGC for providing financial assistance.

References

1 P. Simon and Y. Gogotsi, *Nat. Mater.*, 2008, 7, 320–329.
2 F. Zhu, H. Bao, X. Wu, Y. Tao, C. Qin, Z. Su and Z. Kang, *ACS Appl. Mater. Interfaces*, 2019, **11**, 43206–43213.

3 M. Lechartier, L. Porcarelli, H. Zhu, M. Forsyth, A. Guéguen, L. Castro and D. Mecerreyes, *Mater. Adv.*, 2022, **3**, 1139–1151.
4 M. Armand and J.-M. Tarascon, *Nature*, 2008, **451**, 652–657.
5 C. Hu, Y. Shen, M. Shen, X. Liu, H. Chen, C. Liu, T. Kang, F. Jin, L. Li, J. Li, Y. Li, N. Zhao, X. Guo, W. Lu, B. Hu and L. Chen, *J. Am. Chem. Soc.*, 2020, **142**, 18035–18041.
6 Y. Kato, S. Hori, T. Saito, K. Suzuki, M. Hirayama, A. Mitsui, M. Yonemura, H. Iba and R. Kanno, *Nat. Energy*, 2016, **1**, 1–7.
7 I. Garagounis, V. Kyriakou, C. Anagnostou, V. Bourganis, I. Papachristou and M. Stoukides, *Ind. Eng. Chem. Res.*, 2011, **50**, 431–472.
8 Y. Liu, L. Fan, Y. Cai, W. Zhang, B. Wang and B. Zhu, *ACS Appl. Mater. Interfaces*, 2017, **9**, 23614–23623.
9 P. I. Cowin, C. T. G. Petit, R. Lan, J. T. S. Irvine and S. Tao, *Adv. Energy Mater.*, 2011, **1**, 314–332.
10 D. W. Joh, J. H. Park, D. Y. Kim, B.-H. Yun and K. T. Lee, *J. Power Sources*, 2016, **320**, 267–273.
11 Q. L. Liu, S. H. Chan, C. J. Fu and G. Pasciak, *Electrochem. Commun.*, 2009, **11**, 871–874.
12 V. Gil, C. Moure, P. Durán and J. Tartaj, *Solid State Ionics*, 2007, **178**, 359–365.
13 N. Jaiswal, B. Gupta, D. Kumar and O. Parkash, *J. Alloys Compd.*, 2015, **633**, 174–182.
14 T. Tunc, I. Uslu, S. Durmusoglu, S. Keskin, A. Aytimur and A. Akdemir, *J. Inorg. Organomet. Polym.*, 2012, **22**, 105–111.
15 T. Takahashi, T. Esaka and H. Iwahara, *J. Appl. Electrochem.*, 1975, **5**, 197–202.
16 N. M. Sammes, G. A. Tompsett, H. Nafe and F. Aldinger, *J. Eur. Ceram. Soc.*, 1999, **19**, 1801–1826.
17 M. Drache, P. Roussel and J.-P. Wignacourt, *Chem. Rev.*, 2007, **107**, 80–96.
18 E. D. Wachsman, S. Boyapati and N. Jiang, *Ionics*, 2001, **7**, 1–6.
19 D. W. Jung, K. T. Lee and E. D. Wachsman, *J. Electrochem. Soc.*, 2016, **163**, F411–F415.
20 P.-H. Gao, S.-C. Zeng, C. Jin, B. Zhang, B.-Y. Chen, Z. Yang, Y.-C. Guo, M.-X. Liang, J.-P. Li, Q.-P. Li, Y.-Q. Lu, L. Jia and D. Zhao, *Materials*, 2021, **14**(1–15), 7470.
21 K. Vasundhara, S. N. Achary, S. J. Patwe, A. K. Sahu, N. Manoj and A. K. Tyagi, *J. Alloys Compd.*, 2014, **596**, 151–157.
22 E. D. Wachsman and K. L. Duncan, *Electrochem. Soc.*, 1999, **19**, 264–274.
23 J.-Y. Park and E. D. Wachsman, *Ionics*, 2006, **12**, 15–20.
24 X. Gao, Y. Shang, L. Liu and K. Gao, *J. Alloys Compd.*, 2019, **803**, 565–575.
25 S. Majeed and S. A. Shivashankar, *J. Mater. Chem. C*, 2014, **2**, 2965–2974.
26 Z. Wang, H. Du, Z. Liu, H. Wang, A. M. Asiri and X. Sun, *Nanoscale*, 2018, **10**, 2213–2217.
27 Q. He, Y. Ni and S. Ye, *RSC Adv.*, 2017, **7**, 27089–27099.
28 M. S. Athar, M. Danish and M. Muneer, *J. Environ. Chem. Eng.*, 2021, **9**, 105754.
29 S. S. Raut, O. Bisen and B. R. Sankapal, *Ionics*, 2017, **23**, 1831–1837.
30 N. Zeeshan and Rafiuddin, *Measurement*, 2019, **138**, 1–7.
31 S. Cui, R. Li, C. Zhu, J. Pei and Y. Wen, *Sep. Purif. Technol.*, 2020, **239**, 116520.
32 F. Chen, X. H. Zhang, X. D. Hu, W. Zhang, R. Zeng, P. D. Liu and H. Q. Zhang, *J. Alloys Compd.*, 2016, **664**, 311–316.
33 M. S. Pujar, S. M. Hunagund, V. R. Desai, S. Patil and A. H. Sidarai, *AIP Conf. Proc.*, 2018, **1942**, 050026.
34 S. Imteyaz and Rafiuddin, *RSC Adv.*, 2015, **5**, 96008.
35 Y. A. S. Khadar, A. Balamurugan, V. P. Devarajan and R. Subramanian, *Orient. J. Chem.*, 2017, **33**, 2405–2411.
36 S. Imteyaz and Rafiuddin, *J. Mol. Struct.*, 2016, **1123**, 116–123.
37 E. Radvanyi, K. V. Havenbergh, W. Porcher, S. Jouanneaua, J.-S. Bridel, S. Put and S. Franger, *Electrochim. Acta*, 2014, **137**, 751–757.
38 S. Sultana and Rafiuddin, *J. Alloys Compd.*, 2011, **509**, 9842–9848.
39 A. R. C. Bredar, A. L. Chown, A. R. Burton and B. H. Farnum, *ACS Appl. Energy Mater.*, 2020, **3**, 66–98.
40 M. Z. Iqbal and Rafiuddin, *Ceram. Int.*, 2015, **41**, 13650–13657.
41 D. C. Onwudiwe, T. Arfin and C. A. Strydom, *Electrochim. Acta*, 2014, **127**, 283–289.
42 P. Sharma, D. K. Kanchan, M. Pant, M. S. Jayswal and N. Gondaliya, *New J. Glass Ceram.*, 2011, **1**, 112–118.
43 J. A. Dias, S. H. Santagneli and Y. Messaddeq, *J. Phys. Chem.*, 2020, **124**(49), 26518–26539.
44 N. Gondaliya, D. K. Kanchan, P. Sharma and M. S. Jayswal, *Polym. Compos.*, 2012, **33**, 2195–2200.
45 Y. L. Yap, A. H. You, L. L. Teo and H. Hanapei, *Int. J. Electrochem. Sci.*, 2013, **8**, 2154–2163.
46 M. L. Verma, M. Minakshi and N. K. Singh, *Ind. Eng. Chem. Res.*, 2014, **53**, 14993–15001.
47 A. M. Stephan, *Eur. Polym. J.*, 2006, **42**, 21–42.
48 S. I. Wani and Rafiuddin, *Electrochim. Acta*, 2020, **342**, 136097.
49 M. Thambidurai, N. Muthukumarasamy, D. Velauthapillai, S. Agilan and R. Balasundaraprabhu, *Powder Technol.*, 2012, **217**, 1–6.
50 B. P. Dubey, A. Vinodhkumar, A. Sahoo, V. Thangadurai and Y. Sharma, *ACS Appl. Energy Mater.*, 2021, **4**, 5475–5485.
51 H.-M. Li, C.-H. Ra, G. Zhang and W. J. Yoo, *J. Korean Phys. Soc.*, 2009, **54**, 1096–1099.
52 M. Z. Iqbal and Rafiuddin, *Measurement*, 2016, **81**, 102–112.
53 D. M. Abdel-Basset, S. Mulmi, M. S. El-Bana, S. S. Fouad and V. Thangadurai, *Inorg. Chem.*, 2017, **56**, 8865–8877.
54 M. Ram, *Physica B*, 2010, **405**, 1359–1361.
55 N. S. Salami and S. Beg, *J. Alloys Compd.*, 2014, **586**, 302–307.
56 R. Ahmed, A. S. M. Moslehuddin, Z. H. Mahmood and A. K. M. A. Hossain, *Mater. Res. Bull.*, 2015, **63**, 32–40.
57 D. Maurya, J. Kumar and Shripal, *J. Phys. Chem. Solids*, 2005, **66**, 1614–1620.
58 G. C. Psarras, E. Manolakaki and G. M. Tsangaris, *Composites, Part A*, 2002, **33**, 375–384.